

27 pT Silicon Nitride MEMS Magnetometer for Brain Imaging

Kushagra Sinha and Massood Tabib-Azar

Abstract—We report the design, fabrication, and characterization of an ultrasensitive resonant (~ 300 – 400 Hz) magnetometer with 0.67 -mV/nT sensitivity. The sensor was composed of a low stress (-14 MPa) low-pressure chemical vapor deposition silicon nitride cross bridge and a neodymium magnet. External magnetic field biasing (to modify the effective Hooke's constant), shielding, mechanical isolation, and parametric amplification and feedback were used to progressively improve the sensor performance from 1 μ T minimum detectable signal to 27 pT; an improvement of five orders of magnitude. The sensor's average temperature sensitivity around the room temperature was 11.9 pV/pT/°C.

Index Terms—MEMS, magnetometer, parametric amplification.

I. INTRODUCTION

ULTRASENSITIVE, room temperature magnetometers with 10 fT minimum detectable signal (MDS) are required for magneto-encephalography (MEG), to image and connect our brain circuitry and firing patterns to our behavior. Atomic vapor, high-temperature, superconducting quantum interference devices (SQUIDS), and very high sensitivity micro-electromechanical systems (MEMS) magnetometers are being developed for these and related applications [1]. Magnetic fields in the brain are produced by electric currents flowing in 10^3 – 10^6 bundles of axons. When co-fired, these bundles produce 10 fT to 10 pT magnetic flux density a few centimeters away at the surface of the skull [2]–[5]. Although the origin of MEG and electroencephalography (EEG) is the same, some have suggested that magnetic fields are not affected by different layers of the brain tissue that affect the EEG signals, potentially enabling higher spatial resolution in MEG. On the other hand, EEG is much easier to detect and is readily used during regular daily activities to understand brain circuitry and its relationship to behavior. MEG signals based on SQUIDS are weaker and require longer integration time that reduce its temporal resolution. The main objective of the work reported here is to develop room temperature magnetometers, with the potential applications in mapping brain activities, in behaving humans in our natural

environment with the hope of learning and discovering neuron firing patterns and their relationship with our behavior.

Magnetometers have been developed extensively during the past five decades. The Lorentz force, the Hall Effect, AMR, GMR, magnetostriction, the magnetoresistive effect and flux gate are some of the commonly used transduction techniques reported. Li *et al.* [6] reported a Lorentz force magnetometer for an electronic compass with a resolution of 210 nT/ $\sqrt{\text{Hz}}$ operating using a DC supply of 2 V at 21.29 KHz resonance frequency. In the recent past a new approach for sensor fabrication has been used. Magnetoelectric composites have been used by Marauska *et al.* [7] as cantilever deposit to give a minimum resolution of 30 pT and sensitivity of 3.8 V/mT. Using a bias current of 7.245 mA, Kumar *et al.* [8] reported the sensitivity of a Lorentz force magnetometer device to be 2.107 mV/nT, considering a low noise floor of 2.8 pT/ $\sqrt{\text{Hz}}$. A Lorentz force based, torsional resonant magnetometer has been reported by Ren *et al.* [9], that had a sensitivity of 400 mV/ μ T and a resolution of up to 30 nT in 10 Pa vacuum. Kádár *et al.* [10] reported a magnetometer with 1 nT sensitivity using a device dimension of 2800 $\mu\text{m} \times 1400$ μm . The Lorentz force sensors have the advantage of being hysteresis free when compared to the magnetoresistive and the flux gate magnetometers. Haned and Missous [11] used Hall Effect to sense magnetic flux density variation and were able to achieve 100 nT resolution using AC technique. Bertoldi *et al.* [12] used anisotropic magnetoresistive effect (AMR) as the transduction technique to detect the magnetic field changes as small as 20 nT. Giant magnetoresistance effect (GMR) was used by Wang *et al.* [13] to achieve a resolution level of 30 nT. Liakopoulos and Ahn [14] used the micro-fluxgate principle to detect a minimum of 60 nT signal, and they used 3D toroidal type planar coils 5 mm \times 2.5 mm for detection and excitation. Yabukami *et al.* [15] reported a high frequency carrier-type sensor with 88 pT sensitivity using giant magneto-impedance effect (GMI).

Here we discuss a ferromagnetic MEMS magnetometer composed of a low compressive stress (-14 MPa) silicon nitride devices with a Neodymium rare earth magnet as the foot-mass. An external DC magnetic flux and a feedback signal were used to respectively bias the devices and parametrically amplify the AC magnetic field input signal, improving the sensor sensitivity by 350 times (from 1.9 μ V/nT to 0.67 mV/nT) and its MDS by 4 orders of magnitude (from 1 μ T to 27 pT). We have reported a fiber optic magnetometer with sub pT sensitivity in the past [16]. To improve the sensor's sensitivity and MDS, we are further reducing its effective elastic constant, its mass, and the RMS noise level. Table.1 below shows the

Manuscript received January 26, 2016; revised June 13, 2016; accepted June 14, 2016. Date of publication June 16, 2016; date of current version August 3, 2016. This work was supported by the National Science Foundation through the Early-Concept Grants for Exploratory Research Program under Grant 1419836. The associate editor coordinating the review of this paper and approving it for publication was Dr. Tony Huang.

K. Sinha is with the University of Utah, Salt Lake City, Utah 84112 USA (e-mail: u0931097@utah.edu).

M. Tabib-Azar is with the University of Utah, Salt Lake City, Utah 84112 USA. He is now on sabbatical with the Electrical Engineering and Computer Science Department, University of California at Berkeley, Berkeley, CA 94704 USA (e-mail: azar@berkeley.edu).

Digital Object Identifier 10.1109/JSEN.2016.2582039

TABLE I
COMPARISON OF THE MAGNETOMETERS
REPORTED BY VARIOUS GROUPS

S.no	Authors	Type	Sensitivity	MDS	Device Dimensions
1.	This work	Ferromagnetic	0.67 mV/nT	27 pT	8000 × 2000 × 1.5 (μm) ³
2.	Marauska <i>et al.</i> [14]	Magneto-Electric	0.0038 mV/nT	30 pT	200 × 900 × 7.8 (μm) ³
3.	Yabukami <i>et al.</i> [15]	GMI	-	88 pT	5000 × 50 (μm) ²
4.	Kádár <i>et al.</i> [10]	Lorentz Force	23.7 V ² /mT	1 nT	2800 × 1400 (μm) ²
5.	Bertoldi <i>et al.</i> [12]	AMR	10 mV/V/ mT	20 nT	1000 × 1000 (μm) ²
7.	Wang <i>et al.</i> [13]	GMR	2.73 mV/ V/ Oe	30 nT	1400 × 1400 (μm) ²
8.	Liakopoulos and Ahn [14]	Micro-Fluxgate	0.008 mV/nT	60 nT	5000 × 2500 (μm) ²
9.	Kumar <i>et al.</i> [8]	Lorentz Force	2.1 mV/nT	0.28 pT	800 × 800 × 1.5 (μm) ³
10.	Ren <i>et al.</i> [3]	Torsional MEMS	0.4 mV/nT	30 nT	400 × 20 × 60 (μm) ³
11.	Mo Li <i>et al.</i> [5]	Torsional MEMS	1.03 X10 ⁻⁵ mV/nT	60 nT	1060 × 800 × 30 (μm) ³
12.	Nguyen <i>et al.</i> [2]	Quartz MEMS	6.36 X10 ⁻⁵ mV/nT	250 μT	600 × 400 × 2.5 (μm) ³

comparison of the sensitivity and the minimum detectable signal (MDS) between our sensor and sensors reported by other groups.

II. DESIGN

The MEMS sensor design for measuring ultra-low magnetic flux density of the order of 10 fT, requires a large signal/displacement, for a very small applied force (i.e., large X/F). We examined four different structures; i) cross-bridge (device# 1), ii) 3-leg bridge (device #2), iii) a regular bridge, and iv) a diaphragm (Fig. 1). All these structures were tested with a neodymium rare earth magnet placed at their center. The Hooke's constant of the device, calculated from its resonant frequency, was a function of the mass of the magnet (12-24 mg) and the built-in-stress (ϵ) as $k = \frac{AEt^3w}{l^3}$ and $\epsilon \propto E$.

The device #1 (Fig. 1a), was found to have most stable output response whereas the device #2 (Fig. 1b) yielded the maximum output per unit force (presumably due to its lower spring constant compared to device #1). The device#3 (Fig. 1c) was unstable due to the magnet mass that tilted and resulted in loss of laser reflection at resonance. The device #4, a diaphragm structure (Fig. 1d) was stable but had lower sensitivity.

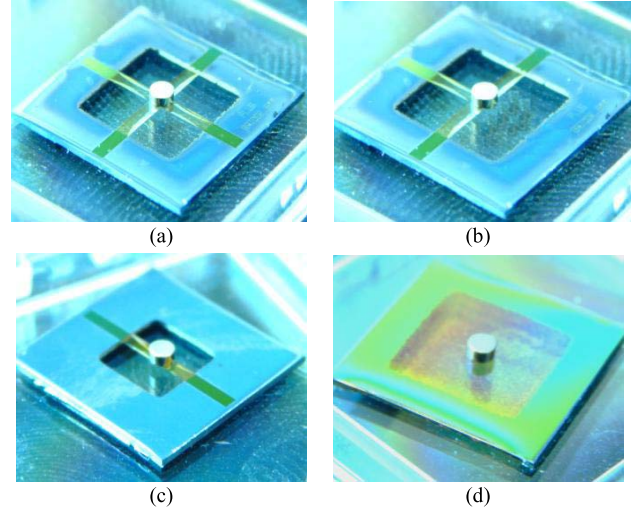


Fig. 1. Optical image of the MEMS devices: (a) plus-bridge (device #1); (b) 3-leg bridge (device #2); (c) bridge (device #3); (d) diaphragm (device #4) designed and fabricated to sense ultra-low magnetic flux density.

The dynamics of a MEMS structure [17]–[19] is given by eq. (1). The damping coefficient (b) and the spring constant (k) were varied with external bias, magnet mass (M), and the built-in stress. The parameters were adjusted to get the maximum response (displacement/input magnetic field) for a given force on the sensor due to the external magnetic field. The equation of motion for the flexure sensor is given by:

$$F = M\ddot{x} + b\dot{x} + kx \quad (1)$$

where ' F ' is the overall force acting on the sensor and ' x ' is the net resultant displacement. We note that for a simple harmonic excitation ($F \sim F_0 e^{i\omega t}$), the displacement and its derivatives are given by:

$$\begin{aligned} x &= x_0 e^{i(\omega t + \theta)}, \\ \dot{x} &= i\omega x_0 e^{i(\omega t + \theta)} = i\omega x, \\ \ddot{x} &= -\omega^2 x_0 e^{i(\omega t + \theta)} = -\omega^2 x, \end{aligned} \quad (2)$$

where x_0 is:

$$x_0 = \frac{F_0/k}{\left[\left(1 - \frac{\omega^2}{\omega_0^2} \right) + i \left(\frac{\omega}{Q\omega_0} \right) \right]} \quad (3)$$

with

$$|x_0| = \frac{F_0/k}{\sqrt{\left(1 - \frac{\omega^2}{\omega_0^2} \right)^2 + \left(\frac{\omega}{Q\omega_0} \right)^2}}$$

and

$$\theta = \tan^{-1} \left[\frac{\left(\frac{\omega}{Q\omega_0} \right)}{\left(1 - \frac{\omega^2}{\omega_0^2} \right)} \right] \quad (4)$$

where $\omega_0 = \sqrt{\frac{k}{M}}$ and ' Q ' is the quality factor ($Q = \frac{M\omega_0}{b}$). The weight of the device, in our case, was dominated by the magnet mass that was much larger than the mass of the

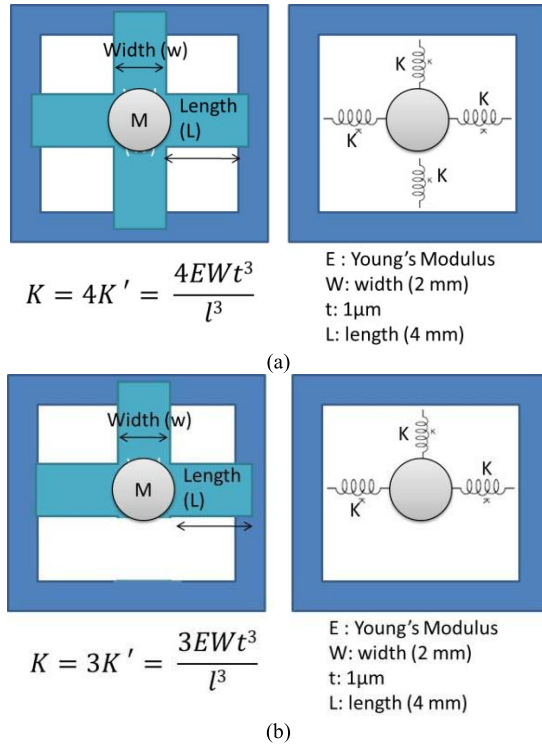


Fig. 2. Schematic of the (a) device# 1 and (b) device #2 and its simple model showing the effective Hooke's constant of the sensor. The built-in stress was not considered for theoretical calculations and that its effect on resonance frequency change was evaluated by experimentation and simulation.

silicon nitride bridge. Fig. 2 shows schematic of two of our sensors, their mechanical models, and expressions for their effective Hooke's constants and sensors' dimensions. The permanent magnet causes the bridge to sag near the center due to the gravity as shown in Fig. 3a. The tension caused by the sagging changes the effective Hooke's constant of the bridge and modifies its resonance frequency. Using an external magnet, one can modify the amount of sagging and increase or decrease the effective Hooke's constant as shown in Figs. 3b and 3c.

In addition to the magnetic field biasing, we used parametric feedback to improve our sensors' performance. We note that an additional force F_1 can be added to the overall force: $F = F_0 e^{i\omega t} + F_1$ to enable additional modification of the sensor's dynamics as follows. If $F_1 \sim k_f x$, with k_f an appropriate constant, F_1 will clearly change the Hooke's constant of the sensor to $k - k_f$. Likewise, if $F_1 \sim b_f \dot{x}$ with b_f another appropriate constant, the effective damping coefficient will become $b - b_f$. Or, if $F_1 \sim m_f \ddot{x}$, then the mass will be modified as $M - m_f$. So, by choosing the correct F_1 we can modify almost all the important parameters of the sensor. To produce these F_1 's, all we need to do is to take the sensors' output and electronically convert it to a signal that is proportional to x or its derivatives as shown in (2). Noting that $i \sim e^{i\pi/2}$, $F_1 \sim b_f \dot{x} = i \left[\omega \left(\frac{b_f}{\omega} \right) \right]$ can be easily generated by taking the position signal and phase shifting it by $\pi/2$. Likewise, phase shifting the position signal by π , produces a signal proportional to \ddot{x} . The multipliers ω in the first case and ω^2 in the second case are simply part of the b_f and m_f .

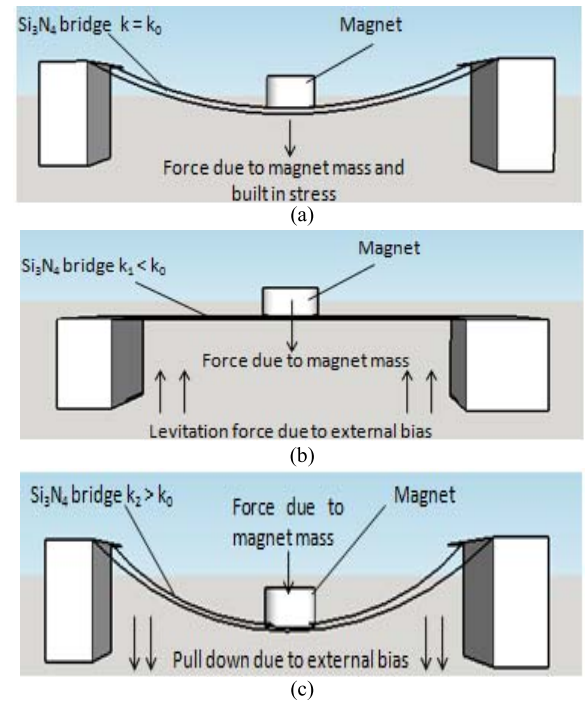


Fig. 3. a) The weight of the permanent magnet applies tension to the bridge and modifies its spring constant. (b) With an external magnetic field of $+13.75 \text{ mT}$, the tension can be nulls, (c) With an external field of -13.75 mT , the tension can be increased.

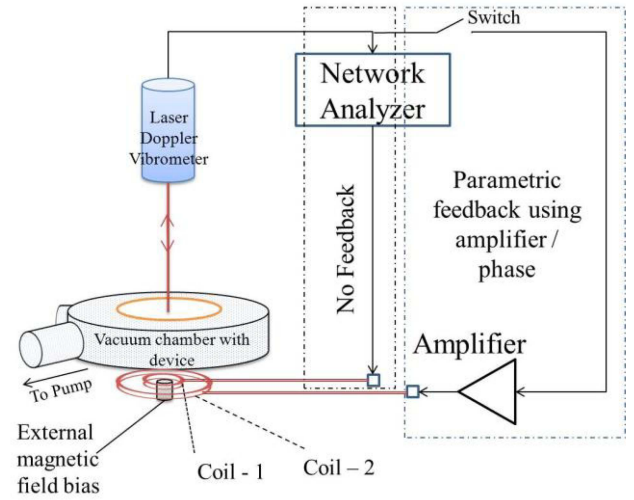


Fig. 4. Schematic of experimental set-up. The laser was reflected off the sensor. The gap between the coils and the device was 2.5 cm and was varied to study effect of lower magnetic flux density.

Thus, this method of modifying the sensor's dynamics only works near resonance, when the displacement signal is largest. The phase shifts are simply produced by a band-pass filter with the correct 3 dB frequencies, that is an integral part of a feedback amplifier, as schematically shown in Fig. 4.

The above improvements along with the sensor isolation and flux concentrator were used to achieve the 27 pT MDS as discussed next, after discussing the sensor fabrication and characterization.

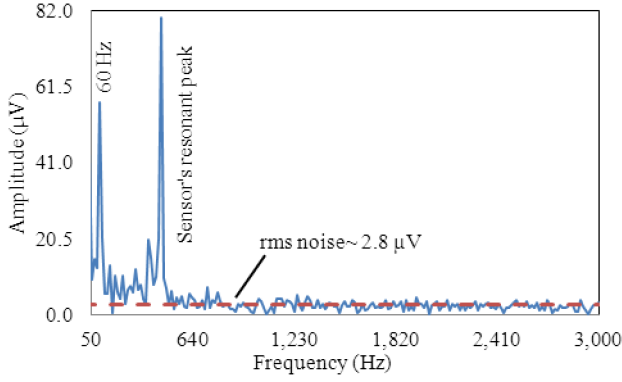


Fig. 5. Output voltage spectrum of the device #1 showing RMS noise floor of 2.8 μV . Input to the inner coil (Fig. 4) was fixed at 0.07 nT. Bandwidth was 2 Hz. RMS noise level was calculated from 638 HZ to 3 KHz.

III. FABRICATION

The sensors were fabricated on a double sided polished Si wafer that was cleaned and thermally oxidized to form 500 nm of SiO_2 by wet oxidation, at 1050 $^\circ\text{C}$, that introduced a compressive stress of 300 MPa. Next, low pressure chemical vapor deposition (LPCVD) of silicon nitride was used to deposit a 1-2 μm thick silicon rich nitride layer at 825 $^\circ\text{C}$. The stress in this layer was 128 MPa tensile. The oxide and nitride had a combined compressive stress of ~ 14 MPa. The nitride was then patterned and etched using 50 sccm of CF_4 and 5 sccm of O_2 at 15 $^\circ\text{C}$ to produce cross bridges, bridges and diaphragms. Finally, using Al metal mask on the back, DRIE using SF_6 and C_4F_8 was used to release the beams. Subsequently a small Neodymium magnet was attached to their center (Fig. 1).

IV. CHARACTERIZATION

The sensors were tested in 1 mTorr vacuum inside an aluminum sample holder with an optical window. The optical detection techniques for non-contact displacement measurement include beam triangulation [20], interferometry [21]–[23] and Doppler vibrometry [24]. Here we used a Doppler vibrometer to measure sensor displacement and a network analyzer to excite the device through a coil and also to display the vibration amplitudes provided by the vibro meter. The vibro meter output was also electronically modified (amplified and phase shifted) and used as a parametric feedback to the sensor, through a second coil, as schematically shown in the Fig. 4.

A. Sensor Response

The device response, shown in Fig. 5, was measured by applying 0.07-1.1 nT (14-200 μA) excitation to the external coil (\varnothing 5 cm) (Fig. 4). The force acting on the sensor (F) with permanent magnetic dipole ' m ' and an external magnetic flux density ' B ' is given by:

$$F = \nabla(m \cdot B) \quad (5)$$

In our experiments, the magnet was directly above the coil near its center. So, we can use the z-component of the ' B ' and ' m ' and replace the ' ∇ ' operator with ' $\frac{\partial}{\partial z}$ '. We further note that the magnetic flux density of a disk shaped permanent

magnet along its axis (z-component) is approximately given by:

$$B_{zmagnet}(surface) = B_s = \frac{\mu_0 m}{V_m}, \quad (6.a)$$

where the volume of the magnet is denoted by ' V_m ' and $\mu_0 = 4\pi \times 10^{-7}$ Henry/m. The surface magnetic flux density (B_s) in our devices were around 1 mT. We also note that the magnetic field along the axis of a coil with N turns and radius ' r ' is given by:

$$B_{zcoil} = \frac{\mu_0 N I}{2} \frac{r^2}{(r^2 + z^2)^{3/2}} \equiv \frac{r^3 B_0}{(r^2 + z^2)^{3/2}} \quad (6.b)$$

where ' z ' is the distance between the sensor's magnet and the center of the coil, $B_0 = \frac{\mu_0 N I}{2r}$ is the magnetic flux density at the center of the coil, and $I = \frac{V_0 \cos(\omega t)}{R}$ represents the current passed through the coil, in series with a resistor (R) at radial frequency (ω) connected to a voltage source with peak output voltage of ' V_0 '. Thus, the force on the sensor is given by: $F_{z-sensor} = \frac{\partial (V_m B_s B_{zcoil} / \mu_0)}{\partial x} = \frac{-3zr^3 V_m B_s B_0}{\mu_0 (r^2 + z^2)^{5/2}}$.

The negative sign indicates that the force decreases as ' z ' becomes larger. The force has a ' $\frac{1}{z^4}$ ' dependence. It is easy to see that for $B_0 \sim 1$ nT, $r \sim 5$ cm, $z \sim 2.5$ cm, $V_m \sim 1$ mm³, $B_s \sim 0.1$ mT, we get $F \sim 0.1$ nN. So the sensor should be sensitive enough to produce an output voltage above the noise level with 0.1 nN force (Fig. 5). The displacement of the center of the bridge at can be simply related to the applied force by $x \sim F/k$. So to have a large displacement (response) we need to have a very small spring constant ' k '.

Since the network analyzer had a lower output limit of 0.07 nT/0.707 mV, we increased the distance between the coil and the sensor (2.5-15 cm) keeping the number of turns (18) and radius of the coil constant (\varnothing 3 cm). The sensor sensitivity (S) can be defined as:

$$S = \frac{|x|}{|F|} = \frac{|x|}{|F|} \frac{|F|}{|B|} \quad (7)$$

where the first part of ' S ' is simply ' $1/k$ ' and the second part ($|F|/|B|$) is related to ' B ' through equations 5-6. The sensor output in Fig. 5 was obtained using a laser Doppler vibrometer that produces a signal proportional to the velocity of the bridge ($|dx/dt|$).

Shielding: In order to minimize the effect of stray magnetic fields in our measurements we used high permeability sheets (80% nickel-iron-molybdenum alloy) to cover the device with a small opening at the top for the laser reflection to pass. High μ sheets were also placed below the overall set-up. There was improvement in the output amplitude due to the shielding.

B. External Bias

External magnetic field was used to enable in-situ tuning of the Hooke's constant. When the external field attracted the sensor's magnet, it increased its tensile stress and modified the effective value of the apparent acceleration due to gravity. Both these effects increase the resonance frequency by 14 Hz.

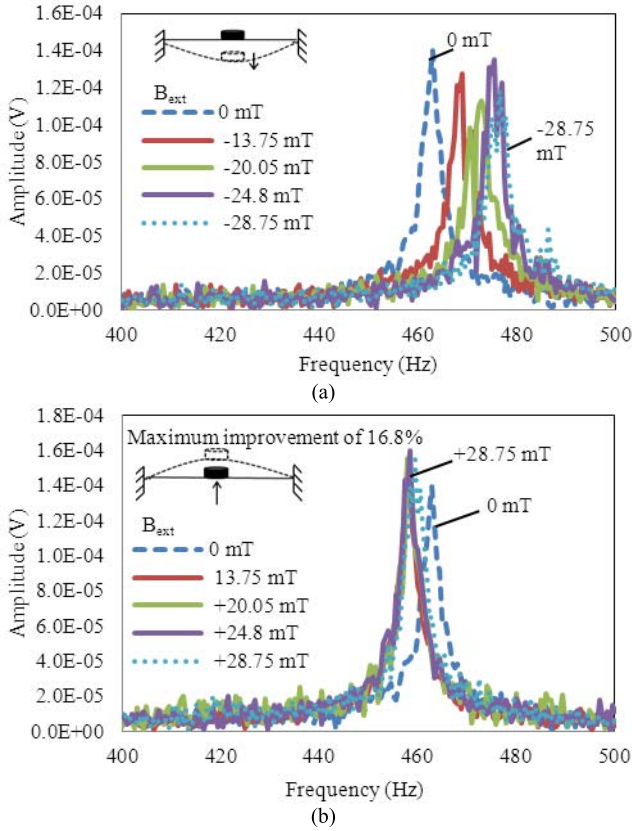


Fig. 6. Sensor (device #1) vibration spectra obtained at different external magnetic fields. (a) When the external field “repelled” the sensor’s magnet, the resonance shifted to lower frequencies and vibration amplitude per unit ac excitation force increased. (b) The opposite was observed when the external field “attracted” the sensor’s magnet.

When the external field “repelled” the sensor’s magnet, it reduced the built-in tensile stress and effectively floated the sensor’s magnet reducing its resonance frequency by 5 Hz. The output amplitude of the sensor decreased in the first case and increased in the second case (Figs. 6a and 6b). The biasing magnetic field improved the sensor output by 11 μV to 24 μV at 463 Hz excitation ($x \sim F/k_{\text{eff}}$). The external magnetic flux (B_{bias}), was varied from -28.75 mT to $+28.75$ mT in the z -direction ($F_{z-\text{sensor}} = \frac{\partial (V_m B_s [B_{z\text{coil}} \pm B_{\text{bias}}/\mu_0])}{\partial z}$).

Table II summarizes the effect of external bias on the vibration amplitude (at resonance) and resonance shift of the device# 1. Although we used permanent magnets to produce the bias field to increase the sensor’s response and lower its resonance, we can easily use a coil and dynamically change the bias field to cope with and cancel the effect of mechanical vibrations on the sensor.

C. Parametric Amplification

To improve the sensitivity of the sensor we used parametric amplification. The term parametric amplification or parametric resonance is an electronic feedback technique that improves both the output ($F \propto B_{\text{eff}}$) and the noise-floor, in resonant structures ($B_{\text{eff}} = B_{z\text{coil}} + B_{\text{feedback}}$). It provides an alternative method that can actuate the resonators, as opposed

TABLE II
EFFECT OF EXTERNAL BIAS ON THE RESONANT
FREQUENCY OF DEVICE #1

External Magnets	Magnetic Flux density (mT)	Amplitude (μV)		Resonant frequency (Hz)	
		-Z polarity	+Z polarity	-Z polarity	+Z polarity
0	0	139.55	139.55	463	463
1	13.75	112.83	150.08	469	458.025
2	20.05	123.93	155.12	473	458
3	24.8	129.67	162.97	476	458.5
4	28.75	133.84	154.24	477	458.5

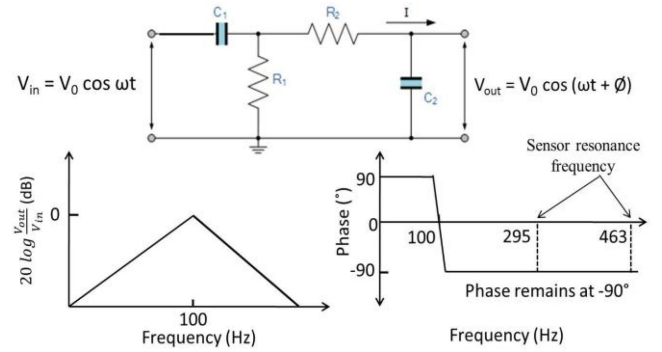


Fig. 7. The band pass filter was used for maximum output generation at 100 Hz. The phase was 0° for 100 Hz and there was a lag of 90° at the resonant frequency.

to the external signal that directly drives the resonator. The spring constant of the resonator varied which in turn modulated the sensor’s response. We then subjected the cross bridge (device# 1) to a 0.07 nT (0.707 mV) input for parametric amplification, and the response of the sensor with increasing gain was studied (Fig. 7). The amplitude increased almost linearly with increasing gain until it saturated at a gain of 200.

For the device #2 the gain was increased while increasing the distance between the coil and the device. For a given stand-off distance (2.5-15 cm), the output was studied only for the maximum gain. Hence, no such relation as shown in the Fig. 8 was obtained for the device #2. We observed maximum output from the sensor at a gain of 200, above which it saturated (Fig. 8). The change increased initially, but saturated at higher gain. The input to the smaller coil (\varnothing 3 cm) was kept constant at 0.07 nT (0.707 mV). We used an averaging of 3 and a bandwidth of 2 Hz for the measurements. Only the device #2 was used to study the effect of parametric amplification. The resonant frequency of the device was 295 Hz, and the amplitude was six times that of the device #1, used for initial characterization. The device dimension was 4 mm \times 2 mm \times 1 μm (Fig. 1b) from the center of gravity. With just three legs, the Hooke’s constant of the device was smaller and the amplitude obtained was much higher, satisfying the equation 3. For parametric amplification measurement, we used 0.07 nT (0.707 mV) as the input to the primary coil, and a bandwidth

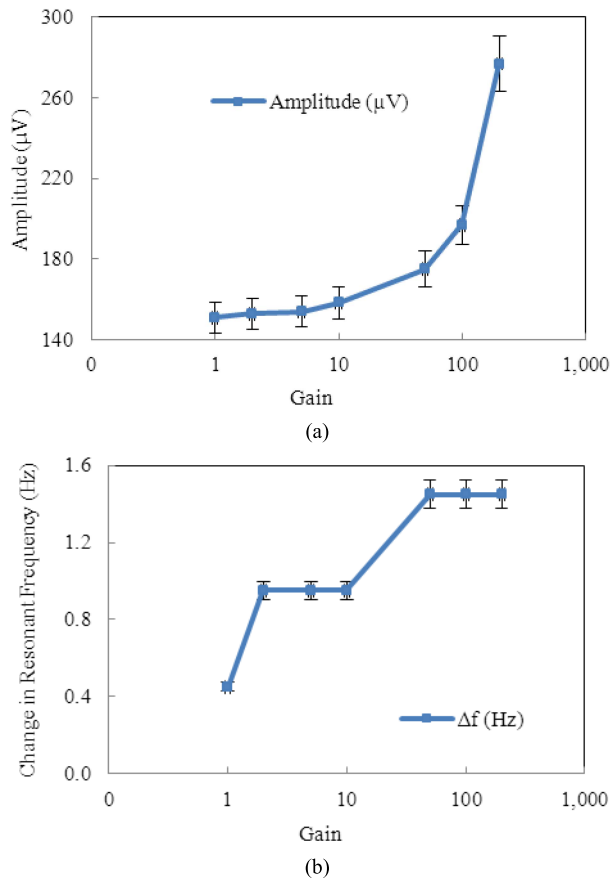


Fig. 8. (a) Peak sensor amplitude at resonance as a function of the gain of the parametric feedback loop. (b) Change in the resonant frequency as a function of the parametric feedback gain. These data were extracted from three averaged spectral measurements with 2 Hz acquisition bandwidth (device# 1).

of 10 Hz. Since, the output was better in the case of 3-leg bridge (device #2), the input magnetic flux density response was studied for lower values by increasing the distance (2.5-15 cm) between the coil and the device. The gain was then adjusted from 10-5000, as the distance was increased from 2.5 cm to 15 cm until it saturated. Using 0.07 nT (0.707 mV) input with 2.5 cm stand-off distance (magnetic flux density of 0.2 nT), the MDS for plus bridge (device #1) was 12.6 nT without feedback and 7 nT for parametric amplification. For the same input excitation and standoff distance between the coil and the device, the MDS for the 3-leg bridge (device #2) were 2 nT and 1 nT which was improved by further decreasing the input magnetic flux density. The amplification used was significant for both the device #1 and the device #2.

The device #1 being a more stable structure was excited with higher magnetic flux density. The device #2 was subjected to lower magnetic flux densities (Fig. 9) by varying the distance between the coil and the device. Parametric amplification was useful as a feedback technique and can be used for many applications in order to increase the MDS of sensors. The effect of external biasing on the inbuilt stress was also shown, using it to increase the amplitude of vibration of the sensor.

The output from the network analyzer was limited to 0.07 nT (0.707 mV). Increasing the distance reduced the

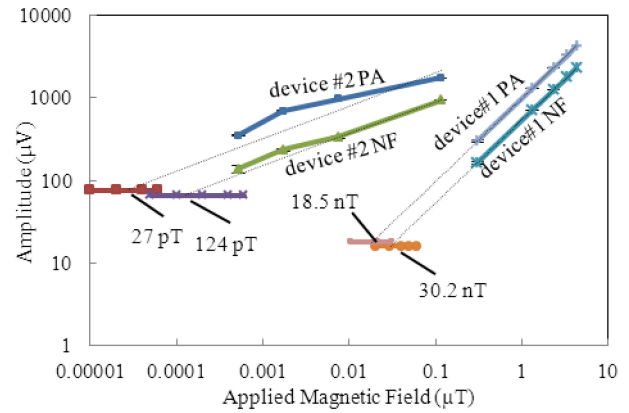


Fig. 9. Graph comparing the MDS and the noise-floor for the device#1 and the device #2 using parametric amplification (PA) and no feedback (NF).

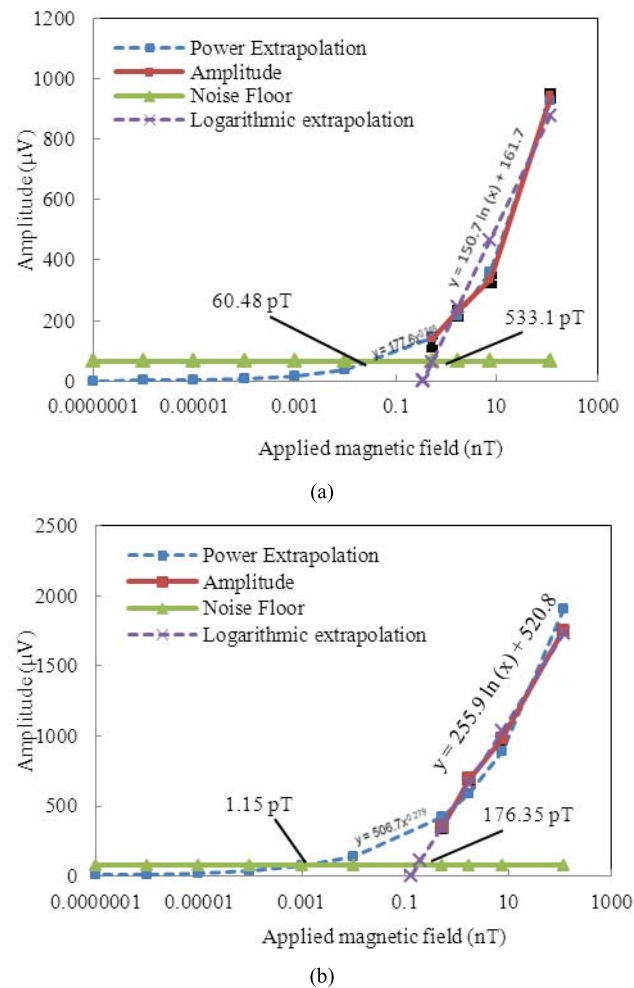


Fig. 10. Graph showing the MDS and the noise-floor for the device #2 (a) without feedback and (b) with parametric amplification.

magnetic field, but for a large distance, a larger shielding box was needed. To obtain the sensor MDS, we extrapolated the sensor output down to its noise-floor (signal-to-noise ratio of 1). We then repeated this procedure with different extrapolation methods (power and logarithmic) (Fig. 10). The MDS of 27 pT was obtained using linear extrapolation. The MDS range for device #2 was 61 pT – 533 pT without

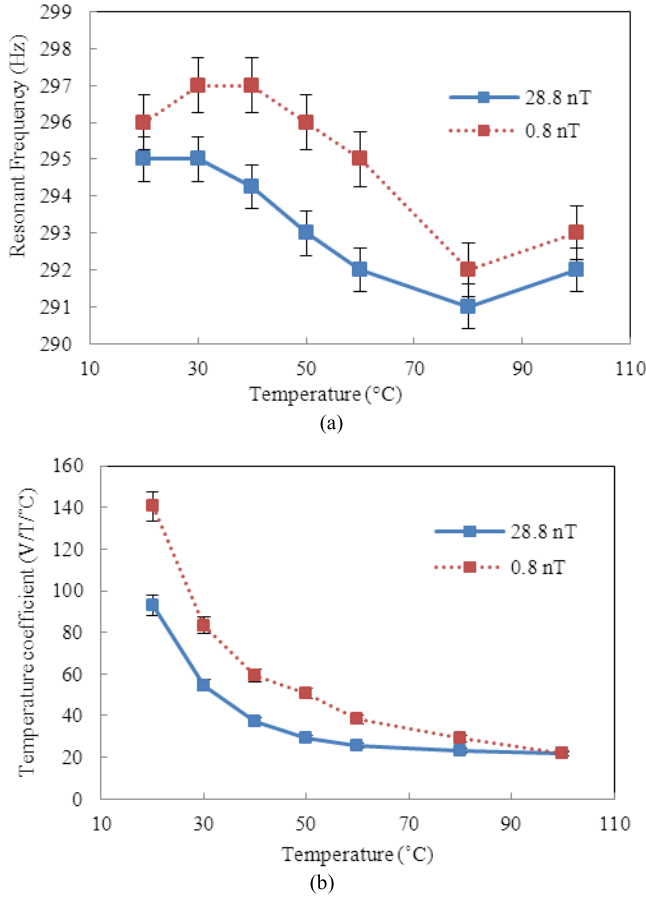


Fig. 11. Temperature variations of the (a) resonant frequency and (b) the sensor output with 0.8 nT and 28.8 nT input applied to the inner coil for device #2. The output was the combined effect of the silicon frame expansion and the silicon nitride structure expansion. We used the smallest and largest excitation values to account for any input magnetic field dependence of the sensor's output variations as a function of temperature.

feedback and 1 pT – 176 pT with parametric amplification. The output, in this case, was for the maximum gain used for each measurement. At 15 cm coil to sensor distance, the minimum input magnetic field detectable was observed. Below 0.02 nT the output of sensor was indistinguishable with noise level. As the input magnetic field decreased, maximum gain at which output saturated increased for the parametric amplification loop. For 0.1 μ T the gain used was just 10, however, for 7 nT, 1 nT and 0.5 nT input the gain used was 100, 500 and 5000 respectively. The extrapolated output for device #2 intersected the noise-floor to give the MDS. The noise-floor, in this case, was measured using the RMS frequency data around the resonant peak, maximizing the effect of parametric amplification. The RMS noise-floor around resonant peak was 77 μ V for parametric amplification (PA) and 67 μ V without any feedback (NF), as the amplitude was higher for PA. Away from the resonant peak, noise-floor was 18.5 μ V for PA and 81.7 μ V for NF.

The resonant frequency of the sensor varied with temperature as can be seen in Fig. 11. The change was 0.05 Hz/°C resulting in 12 pV/pT/°C for 224 mV input. These values were obtained by finding the sensor sensitivity at each temperature (7 different temperatures as shown in Fig. 11) and

calculating its average. We repeated the measurements with lowest and highest available excitation voltages to check for nonlinearities or abnormalities at very small and very large excitation levels.

V. CONCLUSION

In conclusion we used a combination of shielding, external biasing and parametric feedback to demonstrate MEMS magnetometers with MDS of 27 pT and ~ 0.67 mV/nT. The external bias levitating the sensor was shown to increase the sensor's response. Parametric amplification was used to improve the MDS by 4 orders of magnitude and its sensitivity by 350 times.

ACKNOWLEDGMENT

Mr. Rugved Likhite fabricated the nitride bridges.

REFERENCES

- [1] The White House. *Brain Research Through Advancing Innovative Neurotechnologies*, accessed on Dec. 2016. [Online]. Available: <https://www.whitehouse.gov/share/brain-initiative>
- [2] M. Hamalainen, R. Hari, R. J. Ilmoniemi, J. Knuutila, and O. V. Lounasmaa, "Magnetoencephalography theory, instrumentation, and applications to noninvasive studies of the working human brain," *Rev. Modern Phys.*, vol. 65, no. 2, p. 413, 1993. [Online]. Available: <http://journals.aps.org/rmp/abstract/10.1103/RevModPhys.65.413>
- [3] I. Karanasiou, "Functional brain imaging using non-invasive non-ionizing methods: Towards multimodal and multiscale imaging," in *Neuroimaging—Methods*, P. Bright, Ed. Greece: InTech, Feb. 2012.
- [4] R. J. Cooper, N. L. Everdell, L. C. Enfield, A. P. Gibson, A. Worley, and J. C. Hebden, "Design and evaluation of a probe for simultaneous EEG and near-infrared imaging of cortical activation," *Phys. Med. Biol.*, vol. 54, no. 7, pp. 2093–2102, 2009. [Online]. Available: <http://iopscience.iop.org/article/10.1088/0031-9155/54/7/016/meta;jsessionid=049C3367F7AA8E46C572E4CFBF75EC3E.c1.iopscience.cld.iop.org>
- [5] F. Darvas and D. Pantazis, K.-Y. Leahy, "Mapping human brain function with MEG and EEG: Methods and validation," *Neuro Image*, vol. 23, no. 1, pp. S289–S299, 2004. [Online]. Available: <http://www.sciencedirect.com/science/article/pii/S1053811904003799>
- [6] M. Li, V. T. Rouf, G. Jaramillo, and D. A. Horsley, "MEMS Lorentz force magnetic sensor based on a balanced torsional resonator," in *Proc. Transducers Eurosensors XXVII*, 2013, pp. 66–69. [Online]. Available: http://ieeexplore.ieee.org/xpl/articleDetails.jsp?arnumber=6626702&punumber%3D6599514%26filter%3DAND%28p_IS_Number%3A6626676%29%26pageNumber%3D2
- [7] S. Marauska *et al.*, "Highly sensitive wafer-level packaged MEMS magnetic field sensor based on magnetoelectric composites," *Sens. Actuators*, vol. 189, pp. 321–327, Jan. 2013. [Online]. Available: <https://www.infona.pl/resource/bwmeta1.element.elsevier-7343398c-b3b7-35f4-8bb0-77c614dfaa33>
- [8] V. Kumar, M. Mahdavi, X. Guo, E. Mehdizadeh, and S. Pourkamali, "Ultra sensitive Lorentz force MEMS magnetometer with Pico-Tesla limit of detection," in *Proc. 28th IEEE Int. Conf. Micro Electro Mech. Syst. (MEMS)*, 2015, pp. 204–207. [Online]. Available: http://ieeexplore.ieee.org/xpl/login.jsp?tp=&arnumber=7050922&url=http%3A%2F%2Fieeexplore.ieee.org%2Fxppls%2Fabs_all.jsp%3Farnumber%3D7050922
- [9] D. Ren, L. Wu, M. Yan, M. Cui, Z. You, and M. Hu, "Design and analyses of a MEMS based resonant magnetometer," *IEEE Sensors*, vol. 9, no. 9, pp. 6951–6966, Sep. 2009. [Online]. Available: <http://www.mdpi.com/1424-8220/9/9/6951>
- [10] Z. Kádár, A. Bossche, and J. Mollinger, "Integrated resonant magnetic-field sensor," *Sens. Actuators A, Phys.*, vol. 41, nos. 1–3, pp. 66–69, 1994.
- [11] N. Haned and M. Missous, "Nano-Tesla magnetic field magnetometry using an InGaAs-AlGaAs-GaAs 2DEG Hall sensor," *Sens. Actuators A, Phys.*, vol. 102, no. 3, pp. 216–222, Jan. 2006. [Online]. Available: <http://www.sciencedirect.com/science/article/pii/S0924424702003862>

- [12] A. Bertoldi, D. Bassi, L. Ricci, D. Covi, and S. Varas, "Magnetoresistive magnetometer with improved bandwidth and response characteristics," *Rev. Sci. Instrum.*, vol. 76, no. 6, p. 6510695, 2005. [Online]. Available: <http://scitation.aip.org/content/aip/journal/rsi/76/6/10.1063/1.1922787>
- [13] G. A. Wang, S. Arai, T. Kato, and S. Iwata, "Low-drift giant magnetoresistive field sensor using modulation of free-layer magnetization direction," *J. Phys. D, Appl. Phys.* vol. 44, no. 23, p. 235003, May 2011. [Online]. Available: <http://iopscience.iop.org/article/10.1088/0022-3727/44/23/235003/meta>
- [14] T. Liakopoulos and C. H. Ahn, "A micro-flux gate magnetic sensor using micromachined planar solenoid coils," *Sens. Actuators A, Phys.*, vol. 77, no. 1, pp. 66–72, 1999. [Online]. Available: https://www.researchgate.net/publication/223425282_Micro-fluxgate_magnetic_sensor_using_micromachined_planar_solenoid_coils
- [15] S. Yabukami, T. Suzuki, N. Ajiro, H. Kikuchi, M. Yamaguchi, and K. Arai, "A high frequency carrier-type magnetic field sensor using carrier suppressing circuit," *IEEE Trans. Magn.*, vol. 37, no. 4, pp. 2019–2021, Jul. 2011. [Online]. Available: https://www.researchgate.net/publication/224073505_A_high_frequency_carrier-type_magnetic_field_sensor_using_carrier_suppressing_circuit
- [16] P. Pai, L. Chen, and M. Tabib-Azar, "Fiber optic magnetometer with sub-pico tesla sensitivity for magneto-encephalography," in *Proc. IEEE Sensors*, 2014, pp. 722–725. [Online]. Available: http://ieeexplore.ieee.org/xpl/login.jsp?tp=&arnumber=6985101&url=http%3A%2F%2Fieeexplore.ieee.org%2Fxppls%2Fabs_all.jsp%3Farnumber%3D6985101
- [17] S. Timoshenko, D. H. Young, and W. Weaver, Jr., *Vibration Problems in Engineering*, 4th ed. New York, NY, USA: Wiley, 1974.
- [18] S. M. Han, H. Benaroya, and T. Wei, "Dynamics of transversely vibrating beams using four engineering theories," *J. Sound Vibrat.*, vol. 225, no. 5, pp. 935–988, Sep. 1999. [Online]. Available: <http://www.hindawi.com/journals/jam/2011/842805/ref/>
- [19] J. W. Tedesco, W. G. McDougal, and C. A. Ross, *Structural Dynamics: Theory and Applications*. Reading, MA, USA: Addison-Wesley, 1999.
- [20] G. Meyer and N. M. Amer, "Erratum: Novel optical approach to atomic force microscopy," *Appl. Phys. Lett.*, vol. 53, no. 24, p. 2400, 1998. [Online]. Available: <http://scitation.aip.org/content/aip/journal/apl/53/24/10.1063/1.100425>
- [21] T. H. Stievater *et al.*, "Microcavity interferometry for MEMS device characterization," *J. Microelectromech. Syst.*, vol. 12, no. 1, pp. 109–116, 2003.
- [22] W. M. van Spengen, R. Puers, R. Mertens, and I. De Wolf, "Characterization and failure analysis of MEMS: High resolution optical investigation of small out-of plane movements and fast vibrations," *Microsyst. Technol.*, vol. 10, no. 2, pp. 89–96, 2004.
- [23] S. L. Firebaugh, H. K. Charles, Jr., R. L. Edwards, A. C. Keeney, and S. F. Wilderson, "Optical deflection measurement for characterization of microelectromechanical systems MEMS," *IEEE Trans. Instrum. Meas.*, vol. 53, no. 4, pp. 1047–1051, Aug. 2004.
- [24] A. Bosseboeuf and S. Petitgrand, "Characterization of the static and dynamic behavior of M(O) EMS by optical techniques: Status and trends," *J. Micromech. Microeng.*, vol. 13, no. 4, p. S23, 2003.



Kushagra Sinha was born in India on April 23, 1988. He received the undergraduate degree from Bharath University, Chennai, India, in 2011. For his undergraduate study he was awarded Gold Medal by the university. He moved to the University of Utah for his graduate studies in 2014. Currently, he is working towards the Ph. D. degree at the University of Utah, Utah, USA. He is working as a Research Assistant at the AMANDA Laboratory under the guidance of Dr. Massood Tabib-Azar. His major area of study was electronics and instrumentation. He has

worked in the information technology field for 34 months working for CGI Inc. His research interest lies in the field of Microsensors and he is currently working on magnetometers, sensors for Plant health monitoring and energy harvesting.



Massood Tabib-Azar received the M.S. and Ph.D. degrees in electrical engineering from the Rensselaer Polytechnic Institute, in 1984 and 1986, respectively. In 1987, he was a Faculty Member of the EECS Department, Case Western Reserve University. He was a Fellow at NASA in 1992, on Sabbatical at Harvard University from 1993 to 1994, and at Yale University from 2000 to 2001. He is currently a USTAR Professor of ECE with the Electrical and Computer Engineering Department, University of Utah, with adjunct appointment

with the Bioengineering Department. He is on Sabbatical at UC Berkeley from 2015 to 2016. His current research interests include nanometrology (microwave-atomic force microscopy), molecular electronics, novel devices based on solid electrolytes, sensors and actuators (microfluidics), and quantum computing. His teaching interests include development of courses in the area of electronic device physics and electromagnetics with an emphasis on solving problems and the use of computer-aided instruction tools. He has authored three books, two book chapters, over 110 journal publications, and numerous conference proceeding articles. He has introduced and chairs many international symposia in his fields of interest. He was a recipient of the 1991 Lilly Foundation Fellowship and is a member of the New York Academy of Sciences, APS, AAPT, and Sigma Xi research societies. He has also received more than ten certificates of appreciation and recognition for his professional activities and a Best Paper Award from the Design Automation Conference in 2001 for his work on electromagnetic properties of interconnects and defects in ICs.